Requirements for probing chiral Casimir-Polder forces in a molecular Talbot-Lau interferometer

Fumika Suzuki [1,2,*] S. A. Shah,[1,2] Diego A. R. Dalvit,[1] and Markus Arndt [3,†]

[1]*Theoretical Division, Los Alamos National Laboratory, Los Alamos, New Mexico 87545, USA*
[2]*Center for Nonlinear Studies, Los Alamos National Laboratory, Los Alamos, New Mexico 87545, USA*
[3]*University of Vienna, Faculty of Physics& VDSP& VCQ, Boltzmanngasse5, A-1090 Vienna, Austria*

We theoretically investigate the influence of chiral Casimir-Polder (CP) forces in Talbot-Lau interferometry, based on three nanomechanical gratings. We study scenarios where the second grating is either directly written into a chiral material or where the nanomask is coated with chiral substances. We show requirements for probing enantiospecific effects in matter-wave interferometry in the transmission signal and the interference fringe visibility, which depend on the de Broglie wavelength and the molecular chirality. The proposed setup is particularly sensitive to CP forces in the nonretarded regime where chiral effects can be comparable in magnitude to their electric and magnetic counterparts. While the first and third gratings do not change the phase of the matter wave, applying a coating of chiral substances to them enhances the instrument's chiral selectivity.

I. INTRODUCTION

Chirality-dependent dispersion forces, such as the van der Waals (vdW) forces, the Casimir-Polder (CP) forces, and the Casimir effects have been theoretically predicted and analyzed in many prior studies, more recently also with a growing attention towards their experimental detection [1–7]. A better understanding of these interactions promises deeper insight into quantum field theory [3]. Enantiospecific interactions are also important in the understanding of Hund's paradox [8–10] and of homochirality, i.e., the question of why many biomolecules in nature appear with only one chirality [11].

Recent studies of chirality span a diverse range of topics, including chirality-induced spin selectivity [12,13], proximity-induced chiral quantum light [14], induced chirality in clusters [15], circular dichroism in carbon nanotubes [16], chiral AC Stark effects [17], and chiral resonance energy transfer [18]. Although enantiospecific *optical* forces have been observed experimentally [19–23], the detection of chirality-dependent *dispersion* forces has remained a great challenge.

To enhance the sensitivity to *chiral* CP forces, [6] proposed to use slow molecules in electronically excited states and separate enantiomers in a planar chiral cavity. Excited states are appealing as they can exhibit strongly enhanced interaction strengths, but the short lifetime of dipole allowed transitions

also limits the interaction time and the maximal momentum transfer and separation in molecular beam experiments. While the separation and analysis of enantiomers is commonplace in chemistry, our following proposal relies on noncontact distant interactions in high vacuum, which are not commonly accessible. In our present work, we analyze in particular how the interaction of chiral molecules with *chiral* nanogratings influences both the molecular transmission and the molecular fringe visibility in a near-field matter-wave interferometer (see Fig. 1).

The CP potential can be understood as the vdW potential augmented by the influence of retardation [1], and it has already been discussed in the context of matter-wave diffraction of neutral atoms [24–28] and nonpolar [29–31] and polar molecules [32]. The phase accumulated by a molecule in transit through a grating depends on the molecular polarizability, anisotropy, dipole moment, conformation, the molecular velocity, as well as the grating slit width, thickness, and shape. The dielectric function of the grating is relevant across all frequencies, and one may also need to account for charge impurities in the grating [32]. The interaction with nanostructures is favorable as *chiral* CP forces decay faster with distance than their electric and magnetic counterparts in the retarded regime. We propose specifically Talbot-Lau interferometry (TLI), as shown in Fig. 1, as a suitable tool to explore proximity effects since TLI can create coherent self-images of several thousand molecular beams in parallel, all with a low velocity normal to the grating wall.

In the following, we study the conditions under which chiral molecules of sufficiently high rotatory strength may be discriminated by the interferometer transmission and fringe visibility. The paper is organized as follows: In Sec. II, we review the theoretical framework to study the influence of CP forces in Talbot-Lau interferometry with three gratings. In Sec. III, we investigate the impact of chiral CP forces when the second grating G_2 is perfectly chiral and show requirements
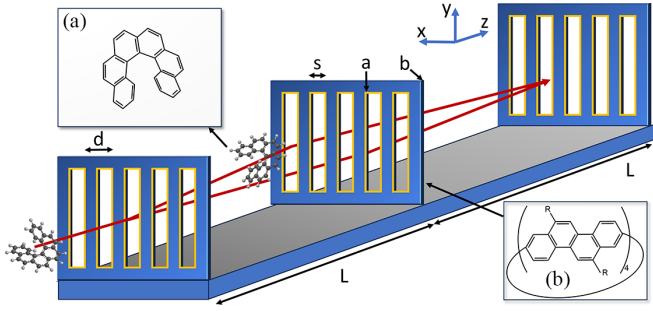
*fsuzuki@lanl.gov
†markus.arndt@univie.ac.at

FIG. 1. A symmetric Talbot-Lau setup consists of three gratings separated by equal distances L. In our present *Gedankenexperiment*, all nanomechanical gratings have a period d, the thickness b, and an open fraction $f = s/d$, where s is the geometrical slit width. The gratings can be made either from inherently chiral material or be written more conventionally into SiN_x and decorated by a layer of chiral substances with thickness a. As an example, we show hexahelicene as the delocalized probe molecule (A) interacting with [4]cyclo- 2,8-chrysenylene (short name [4]CC) as a chiral surface coating (B). Molecules with different properties are discussed in the text.

for observing differences in interferometer transmission and fringe visibility between the enantiomers. In Sec. IV, we study a more realistic scenario where the second grating is inherently non-chiral but coated with chiral substances of high rotatory strength. In Sec. V, we then assume all gratings to be equal and find that chiral coatings of gratings G_1 and G_3 have a strong influence on the enantiomer discriminating power of the instrument, as the chiral CP forces modify the grating transmission function substantially. This can result in observable differences between enantiomers in the total signal strength. Finally, we discuss experimental considerations in Sec. VI and conclude in Sec. VII.

II. CP FORCES IN A TALBOT-LAU INTERFEROMETER

We begin by presenting an overview of the framework employed for studying the effects of CP forces on chiral molecules in a Talbot-Lau interferometer (Fig. 1) composed of three nanogratings, G_1–G_3, each with a thickness of b and a periodicity of d. We choose a grating distance of L. The grating slit width s may be augmented by a chiral coating of thickness a. It can be also reduced by the forces to a cutoff x_c, discussed below. Note that such an interferometer can also be operated with only two gratings, if G_3 is replaced by a molecular binding surface, which can be imaged with 10 nm resolution and high efficiency [33]. Even G_1 could be replaced by a point source.

We start by summarizing the expressions for the expected interferometer signal and fringe visibility and will then add the effect of chiral potentials to the result. This section uses Wigner functions in phase space as described in [34]:

$$w(\mathbf{r}, \mathbf{p}) = \frac{1}{(2\pi\hbar)^2} \int d\mathbf{\Delta}\, e^{i\mathbf{p}\mathbf{\Delta}/\hbar} \rho\left(\mathbf{r} - \frac{\mathbf{\Delta}}{2}, \mathbf{r} + \frac{\mathbf{\Delta}}{2}\right), \quad (1)$$

where $\rho(\mathbf{r}, \mathbf{r}')$ is the position density matrix and $\mathbf{\Delta} = \mathbf{r} - \mathbf{r}'$.

In a Talbot-Lau setup, the molecular beam traverses three gratings G_1–G_3, spaced at equal distances L. The Wigner function after the first grating can be expressed as

$$w_1(\mathbf{r}, \mathbf{p}) = |t_1(\mathbf{r})|^2, \quad (2)$$

assuming that the initial Wigner function is normalized and homogeneous, $w_0(\mathbf{r}, \mathbf{p}) = 1$, i.e., the molecules enter the grating without any prior spatial coherence and evenly from all directions. We further assume a symmetric interferometer where all gratings have the same period d and distance L. The geometrical transmission function can be written as the Fourier series $t_1(x) = \sum_l a_l \exp(2\pi i l x/d)$, where the coefficients a_l depend on the slit width, slit thickness, and coating and also on the interaction between the molecules and the grating wall. We assume a monochromatic molecular beam and will analyze the dependence of the interference fringes on the velocity, i.e., on the de Broglie wavelength.

A free evolution of the molecule over a distance L between the gratings changes the Wigner function,

$$w_1(\mathbf{r}, \mathbf{p}) \rightarrow w_1(\mathbf{r} - L\mathbf{p}/p_z, \mathbf{p}), \quad (3)$$

where p_z is the momentum of the molecule in the z direction. We neglect all external accelerations due to gravity, assuming that all gratings are aligned to better than 100 μrad with the line of gravity. We also neglect the Coriolis acceleration $a_c = 2v \times \Omega_E$ which is about thousand times smaller than the gravitational acceleration for molecules traveling at about 200 m/s, when $\Omega_E = 72$ μrad/s is the frequency of the rotation of the Earth and can be compensated by gravity under suitable interferometer alignment [35].

The passage through each second grating modulates the wave function according to $\psi_1(\mathbf{r}) \rightarrow t_2(\mathbf{r})\psi_1(\mathbf{r})$ where $t_2(\mathbf{r})$ encodes the complex transmission function. The Wigner function after passage through a second grating is thus

$$w_1(\mathbf{r}, \mathbf{p}) \rightarrow \int d\mathbf{q}\, T(\mathbf{r}, \mathbf{q}) w_1(\mathbf{r}, \mathbf{p} - \mathbf{q}), \quad (4)$$

where

$$T(\mathbf{r}, \mathbf{p}) = \frac{1}{(2\pi\hbar)^2} \int d\mathbf{\Delta}\, e^{i\mathbf{p}\mathbf{\Delta}/\hbar} t_2^*\left(\mathbf{r} + \frac{\mathbf{\Delta}}{2}\right) t_2\left(\mathbf{r} - \frac{\mathbf{\Delta}}{2}\right). \quad (5)$$

Talbot-Lau interferometers can generate spatial coherence even from an initially incoherent molecular beam by diffracting the molecules at the slits of the first grating, if the first grating is an absorptive, spatially selective mask, such as a nanomechanical structure or a photodepletion grating [36]. Diffraction within each slit of grating G_1 then prepares the transverse coherence required to achieve spatial superposition and diffraction at G_2. While we can treat G_1 as a pure transmission filter, its CP interaction with the molecule must still be treated carefully. Molecular trajectories are deflected to undetected regions if they pass very close by the grating walls. The effective slit width is thus narrowed by a cutoff distance $2x_c^{(1)}$ which influences both the interference contrast and the transmitted signal. Furthermore, this effect is dispersive: slower molecules are even further deflected and no longer contribute to the signal.

The second grating G_2 then modifies both the amplitude and the phase of the already delocalized matter-wave. In

eikonal approximation the transmission function of the second grating reads

$$t_2(x) \rightarrow t_2(x) \exp\left(-i\frac{mb}{p_z}\frac{V(x)}{\hbar}\right), \tag{6}$$

where m is the mass of the molecule. Note that this additional phase depending on $V(x)$ is canceled out for G_1 and G_3, leaving only the influence of a cutoff induced by the CP force, as discussed below. The quantum coherence term only exists for waves traversing through G_2. Nonetheless, the contribution of G_1 and G_3 to the final signal and visibility is relevant as they modulate the effective transmission.

Assuming that the second grating has the Fourier coefficients b'_m, we find

$$T(x, p) = \int dq \, T_0(x, p - q) T_V(x, q), \tag{7}$$

where

$$T_0(x, p) = \sum_{l,j\in\mathbb{Z}} b'_j b'^{*}_{j-l} \exp\left(2\pi i l \frac{x}{d}\right) \delta\left(p - \hbar\pi\frac{2j-l}{d}\right),$$

$$T_V(x, q) = \frac{1}{2\pi\hbar}\int d\Delta \, e^{iq\Delta/\hbar}$$
$$\times \exp\left\{-i\frac{mb}{p_z\hbar}\left[V\left(x - \frac{\Delta}{2}\right) - V\left(x + \frac{\Delta}{2}\right)\right]\right\}. \tag{8}$$

After free evolution over the distance L, passage through grating G_2, and another free evolution over the distance L, the Wigner function reads

$$w(\mathbf{r}, \mathbf{p}) = \int d\mathbf{q} \left|t_1\left(\mathbf{r} - 2L\frac{\mathbf{p}}{p_z} + \frac{\mathbf{q}}{p_z}L\right)\right|^2 T\left(\mathbf{r} - \frac{\mathbf{p}}{p_z}L, \mathbf{q}\right). \tag{9}$$

We obtain the molecule density by integrating the Wigner function over all momenta and obtain

$$w(x) \propto \sum_{l\in\mathbb{Z}} A_l^* B_{2l}^{(\lambda)} \exp\left(2\pi i l \frac{x}{d}\right). \tag{10}$$

Here, the Talbot coefficients of the first grating are

$$A_l = \sum_{j\in\mathbb{Z}} a_j a_{j-l}^*, \tag{11}$$

while the coefficients of the second grating are

$$B_l^{(\lambda)} = \sum_{j\in\mathbb{Z}} b_j b_{j-l}^* \exp\left(i\pi \frac{l^2 - 2jl}{2}\frac{L}{L_\lambda}\right). \tag{12}$$

Here we have introduced the Talbot length as $L_\lambda = d^2/\lambda$ and the de Broglie wavelength as $\lambda = h/p_z$.

The Talbot coefficients above are modified by the CP potential,

$$b_l = \sum_j b'_j c_{l-j}, \tag{13}$$

where

$$c_l = \frac{1}{d}\int_{-d/2}^{d/2} e^{-2\pi i l x/d}\exp\left(-i\frac{mb}{p_z}\frac{V(x)}{\hbar}\right)dx. \tag{14}$$

This includes the chiral CP potential $V(x)$, which will be discussed below.

While the molecular interference pattern can be captured and imaged on a surface [33,37], for nonfluorescent molecules it has become common to use the spatial resolution of a third transmission mask G_3. The transmitted molecular flux behind G_3 is then a convolution of the density $w(x)$ before the grating and the grating intensity transmission function $|t_3(x)|$:

$$S(x_3) = \int w(x)|t_3(x - x_3)|^2 dx. \tag{15}$$

It then suffices to add a mass-selective large molecule counter [38,39]. The expected signal is then [34]

$$S(x_3) \propto \sum_{l\in\mathbb{Z}} A_l^* A_l'^* B_{2l}^{(\lambda)} \exp\left(2\pi i l \frac{x_3}{d}\right), \tag{16}$$

where A_l' are the Talbot coefficients of the third grating and we extract the sinusoidal fringe visibility

$$\mathcal{V} = \frac{S_{\max} - S_{\min}}{S_{\max} + S_{\min}} = \frac{\left|\sum_{n=1}^{\infty} A_{2n-1} A_{2n-1}' B_{4n-2}^{(\lambda)}\right|}{\frac{1}{2} A_0 A_0' B_0^{(\lambda)} + \sum_{n=1}^{\infty} A_{2n} A_{2n}' B_{4n}^{(\lambda)}}. \tag{17}$$

In the following, we employ these equations to explore the differences in signal and fringe visibility between molecular enantiomers in the presence of chiral CP forces.

Note that molecular orientation is generally relevant in diffraction at nanomechanical masks, since it exposes different components of the polarizability tensor to the grating surface. We assume the chirality to be at a fixed temperature and we average over the molecular orientations.

III. SECOND GRATING WRITTEN INTO A CHIRAL MATERIAL

We start by investigating a scenario in which the second grating is made from a chiral material, characterized by the reflection matrix:

$$\mathbf{R} = \begin{pmatrix} r_{ss} & r_{sp} \\ r_{ps} & r_{pp} \end{pmatrix} = \begin{pmatrix} -r & r_c \\ r_c & r \end{pmatrix}. \tag{18}$$

It describes how the p- and s-polarized components of linearly polarized light, $\mathbf{E}_s$ and $\mathbf{E}_p$, are reflected by the chiral material: $\mathbf{E}_s \rightarrow r_{sp}\mathbf{E}_p + r_{ss}\mathbf{E}_s$ and $\mathbf{E}_p \rightarrow r_{pp}\mathbf{E}_p + r_{ps}\mathbf{E}_s$. For a nonchiral surface, $r_{sp} = r_{ps} = 0$ [40].

The CP potential between the grating and a chiral molecule in the ground state can be expressed as the sum of its electric, magnetic, and chiral components $V = V_e + V_m + V_c$, where [4,41,42]

$$V_e = \frac{\hbar\mu_0}{2\pi}\int_0^\infty d\xi \, \alpha(i\xi)\xi^2 \, \mathrm{tr}\,\mathbf{G}(\mathbf{r}, \mathbf{r}, i\xi),$$

$$V_m = \frac{\hbar\mu_0}{2\pi}\int_0^\infty d\xi \, \beta(i\xi)\,\mathrm{tr}[\nabla \times \mathbf{G}(\mathbf{r}, \mathbf{r}, i\xi)\times \overleftarrow{\nabla}'],$$

$$V_c = -\frac{\hbar\mu_0}{\pi}\int_0^\infty d\xi \, \Gamma(i\xi)\xi \, \mathrm{tr}[\nabla \times \mathbf{G}(\mathbf{r}, \mathbf{r}, i\xi)] \tag{19}$$

and

$$\alpha(i\xi) = \frac{2}{3\hbar} \sum_k \frac{\omega_k |\mathbf{d}_{0k}|^2}{\omega_k^2 + \xi^2}, \quad \beta(i\xi) = \frac{2}{3\hbar} \sum_k \frac{\omega_k |\mathbf{m}_{0k}|^2}{\omega_k^2 + \xi^2},$$

$$\Gamma(i\xi) = -\frac{2}{3\hbar} \sum_k \frac{\xi R_{0k}}{\omega_k^2 + \xi^2}. \tag{20}$$

Here ∇ and $\overset{\leftarrow}{\nabla}'$ act on the first and second position arguments of the Green's tensor only, μ_0 is the vacuum permeability, ω_k the transition frequency, $\mathbf{d}_{0k}$ is the electric dipole transition matrix element, $\mathbf{m}_{k0}$ is the magnetic dipole matrix element, and $R_{0k} = \mathrm{Im}(\mathbf{d}_{0k} \cdot \mathbf{m}_{k0})$ is the optical rotatory strength. Formally, the sum is over all optical transitions [see Eq. (20)] but we can limit the computations to the dominant transition (i.e., $0 \to k = 1$). Both enantiomers have approximately the same modulus but opposite signs of the rotatory strength R_{0k}, and the distinct interference patterns observed between the two enantiomers can be attributed to the different signs of their chiral potential V_c.

The Green's tensor $\mathbf{G}(\mathbf{r}, \mathbf{r}, \omega)$ includes the relevant information about the scattering of photons at the grating walls, and it is written as [43]

$$\mathbf{G}(\mathbf{r}, \mathbf{r}, \omega)$$
$$= \frac{i}{8\pi^2} \int \frac{d^2 k^\|}{k^\perp} e^{2ik^\perp x} \sum_{\sigma_1 \sigma_2 = s, p} r_{\sigma_1 \sigma_2} \mathbf{e}_{\sigma_1}(k^\perp) \mathbf{e}_{\sigma_2}(-k^\perp), \tag{21}$$

where $k^\|$ and $k^\perp$ are the components of the wave vector parallel and perpendicular to the grating surface and $k^{\perp 2} = \omega^2/c^2 - k^{\|2}$. Substituting (20) and (21) into (19), we obtain [4,41,42]

$$V_e(x) = -\frac{r|\mathbf{d}_{01}|^2}{48\pi \epsilon_0 x^3},$$

$$V_m(x) = \frac{r|\mathbf{m}_{01}|^2}{48\pi \epsilon_0 c^2 x^3},$$

$$V_c(x) = \frac{r_c \mu_0 c}{12\pi^2 x^3} R_{01} \ln(\omega_1 x/c), \tag{22}$$

where ϵ_0 is the vacuum permittivity and x is the distance between the molecule and the grating wall. Since we are considering the opening of the grating slit to be around 100 nm in size, we employed the nonretarded limit approximation $x\omega_1/c \ll 1$, which is favorable for the chiral CP potential. In the retarded regime ($x\omega_1/c \gg 1$) the chiral potential ($V_c \propto 1/x^5$) decays faster with distance than its electric and magnetic counterparts ($V_{e,m} \propto 1/x^4$) [4]. Since the molecule is significantly smaller than the grating thickness, we also use the proximity force approximation, wherein a molecule is assumed to interact with the grating as with an infinitely extended surface. The approach and departure of the molecule, i.e., forces acting before and after grating can modify the interference fringes. However, even after including such effects in a careful theory using a Green's function approach [44], every grating model had to be corrected by a fudge factor η in the Casimir force. For a grating with a period of 100 nm, this correction factor shrank from $\eta = 8$ for a grating thickness of 12 nm over $\eta = 5$ for $b = 45$ nm to $\eta = 2$ for $b = 87$ nm. It should be

negligible in our case with $b = 160$ nm. Moreover, all fringe effects and effects of defects in the grating are stationary and even in their presence one can see differences of interactions with molecules of different properties. This was also recently exploited in nanograting interference of molecules with and without electric dipole moments [45]. In our case, the influence of chirality can then be probed differentially by swapping between the enantiomers.

Molecules close to the grating wall are attracted by the dispersive force. If they come within a distance shorter than a cutoff distance x_c, which depends on the materials and their chirality, they may be deflected to beyond the acceptance angle of the detector or even collide with the grating wall. In a typical Talbot-Lau setup, the cutoff distances for the first and second gratings $x_c^{(1)}$ and $x_c^{(2)}$ can be estimated to be

$$\frac{\Delta p_x}{p_z} = \frac{F(x_c^{(1),(2)})\Delta t}{p_z} = \frac{F(x_c^{(1),(2)})mb}{p_z^2} = \theta, \tag{23}$$

where $\theta = 1$ and 2 mrad are common experimental values at the first and second grating, respectively [30]. Here, the force $F(x) = -V'(x)$ is the gradient of the CP potential. For the third grating, $x_c^{(3)}$ is given by [46,47]

$$\frac{b}{v_z} = \sqrt{\frac{m}{2}} \int_0^{x_c^{(3)}} dx \frac{1}{\sqrt{-V(x)}}, \tag{24}$$

where v_z is the longitudinal velocity of the molecule. The chirality dependence of the cutoff distance x_c results in different effective slit openings for different enantiomers. This influences both the interferometer fringe visibility and even more its transmission amplitude.

Since a large optical rotatory strength R_{01} and a large value of r_c result in a strong chiral CP force (22), we consider a beam of molecules whose optical rotatory strength is large compared to their electric and magnetic dipole moment. For the sake of the argument we start by assuming G_2 to be made from a perfectly chiral material. In theory such a structure is conceivable even though it is hard to realize in the laboratory. In that case, $r_c \to 1$ and $r \to 0$, which implies that V_e and V_m vanish and that only the chirality-dependent V_c contributes. A molecule with a positive value of R_{01} is referred to as right-handed and it is attracted to the grating. Its left-handed enantiomer with $R_{01} < 0$ is repelled and only molecules with $R_{01} > 0$ experience a chirality dependent cutoff x_c at a grating of positive chirality.

We therefore expect a difference between two enantiomers in their interferometer transmission and fringe contrast when we include the effect of the chiral CP potential,

$$V(x) = V_c(x + x_o) + V_c(x_o - x), \tag{25}$$

where we let the grating walls be located at $\pm x_o$ with $x_o = fd/2$, and the molecules fly through them, i.e., $x \in (-x_o, x_o)$

Substituting $V(x)$ into (14) and performing the integration including the cutoff x_c, we obtain Fig. 2. Here we let the grating thickness be $b = 160$ nm, the periodicity $d = 257$ nm, the grating distance $L = 50$ mm, and the open fraction $f = 0.45$. These parameters are chosen close to nonchiral nanostructures used in earlier experiments [33]. The top panel shows one period of the matter-wave fringe, i.e., the transmission signal behind $G3$ as a function of the position of the third grating.
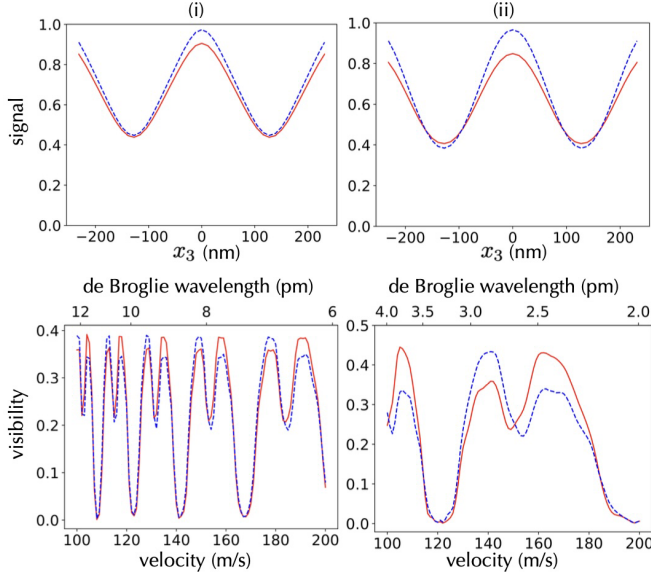
FIG. 2. Predicted interferometer transmission as a function of the position of G_3 (top) and fringe visibility as a function of molecular velocity (bottom). We compare right-handed (solid red line) and left-handed (dashed blue line) molecules. The simulation is done for (i) hexahelicene and (ii) for a hypothetical molecule with $m = 1000$ Da and a rotatory strength ten times greater than that of hexahelicene. Here, the gratings G_1 and G_3 are assumed to be nonchiral while G_2 is assumed to be perfectly right-handed chiral.

This is done both for right-handed (solid red line) and left-handed (dashed blue line) molecules. In the left panel (i), the simulation is performed for hexahelicene with a monochromatic velocity of $v_z = 180$ m/s. Their mass is $m = 328$ Da, and a rotatory strength of $|R_{01}| = 700 \times 10^{-40}$ cgs has been reported with a transition frequency of $\omega_1 = 2\pi \times 10^{15}$ s^{-1} [48]. From such curves we can extract the interference fringe visibility, which we display in the bottom panel as a function of the molecular velocity (bottom scale) and de Broglie wavelength (top scale). The plots show that chirality of hexahelicene can be distinguished in the transmission signal. The panels of column (ii) depict the simulation for a hypothetical molecule with a mass $m = 1000$ Da and a rotatory strength ten times greater than that of hexahelicene with same transition frequency. For the evaluation of the transmission signal, we set $v_z = 140$ m/s. This simulation demonstrates that, due to the chiral CP forces both the interferometer transmission signal and the fringe visibility can differ for opposite enantiomers in well-selected bands of the molecular velocity and de Broglie wavelength.

The figure is the result of numerical computations based on Eqs. (11)–(17), and is in agreement with the expectation that the final signal and fringe visibility must be periodic in the Talbot length and thus the de Broglie wavelength. Electromagnetic properties of the molecules determine an effective open slit width of the grating, which enters the above equations. Due to chiral CP forces, enantiomers perceive different effective forces with the gratings, resulting in slight disparities in signal and visibility even for identical de Broglie wavelengths. This serves as the primary cause of the observed differences between enantiomers, as depicted in the figure.

Note that the assumption so far is strongly idealized: real-world materials generally have $r \neq 0$, and we require that the electric and magnetic anisotropy factor [49] $g_d := |R_{01}/c| / |\mathbf{d}_{01}|^2$ and $g_m := |R_{01} \cdot c| / |\mathbf{m}_{01}|^2$ are sufficiently large to ensure that the chiral CP potential is significant in comparison to its electric and magnetic counterparts (22):

$$r/r_c \leqslant g_e, g_m. \tag{26}$$

A possible solution is to use CP forces with opposite signs for the electric and magnetic components, observed over a perfectly conducting plate [41]. When the magnitudes of $\mathbf{d}_{01}$ and $\mathbf{m}_{01}/c$ are comparable, these two components may cancel, leaving only the chiral component.

Our calculations and similar ones in the literature [2,4,6] rely on an effective-medium approximation, where the spatial variation of permittivity and permeability are neglected. This is only justified when the distance of the molecule to the chiral material exceeds the size of the chiral structure of the metamaterial [50]. This requires nanoscale artifacts inside the grating bars, which is technologically very demanding. To overcome this challenge, in the following section we investigate a scenario where the second grating is coated with chiral molecules.

IV. SECOND GRATING COATED WITH CHIRAL MOLECULES

The electric, magnetic, and chiral components of the CP potential between two molecules can be written as [42,51,52]

$$V_e(x) = -\frac{1}{24\pi^2\epsilon_0^2 x^6} \sum_{k,k'} \frac{\left|\mathbf{d}_{0k}^A\right|^2 \left|\mathbf{d}_{0k'}^B\right|^2}{E_k^A + E_{k'}^B},$$

$$V_m(x) = -\frac{1}{24\pi^2\epsilon_0^2 c^2 x^6} \sum_{k,k'} \frac{\left|\mathbf{m}_{0k}^A\right|^2 \left|\mathbf{m}_{0k'}^B\right|^2}{E_k^A + E_{k'}^B},$$

$$V_c(x) = -\frac{1}{12\pi^2\epsilon_0^2 c^2 x^6} \sum_{k,k'} \frac{R_{0k}^A R_{0k'}^B}{E_k^A + E_{k'}^B}, \tag{27}$$

where the electric dipole transition matrix elements, the magnetic dipole moment matrix elements, the optical rotatory strengths, and the energy differences between the $|0\rangle$ and $|k\rangle$ or $|k'\rangle$ states for molecule A and molecule B are denoted by $\mathbf{d}_{0k}^A$, $\mathbf{d}_{0k'}^B$, $\mathbf{m}_{0k}^A$, $\mathbf{m}_{0k'}^B$, R_{0k}^A, $R_{0k'}^B$, E_k^A, $E_{k'}^B$, respectively. Here, A refers to the molecules propagating as matter waves, while B represents the molecules coating the second grating G_2.

By integrating over all B-molecules in a layer of thickness a and number density n_B, we obtain the potential exerted by the coating:

$$
V_{\text{coat}}(x) = -\frac{n_B}{144\pi\epsilon_0^2}\left(\frac{1}{(x-a)^3} - \frac{1}{x^3}\right)\sum_{m,n}\frac{\left|\mathbf{d}_{0m}^A\right|^2\left|\mathbf{d}_{0n}^B\right|^2}{E_{m0}^A + E_{n0}^B}
$$

$$
-\frac{n_B}{144\pi\epsilon_0^2 c^2}\left(\frac{1}{(x-a)^3} - \frac{1}{x^3}\right)\sum_{m,n}\frac{\left|\mathbf{m}_{0m}^A\right|^2\left|\mathbf{m}_{0n}^B\right|^2}{E_{m0}^A + E_{n0}^B}
$$

$$
-\frac{n_B}{72\pi\epsilon_0^2 c^2}\left(\frac{1}{(x-a)^3} - \frac{1}{x^3}\right)\sum_{m,n}\frac{R_{0m}^A R_{0n}^B}{E_{m0}^A + E_{n0}^B}, \tag{28}
$$

where x is the distance between the molecule and the surface of the grating.

In addition, we include the CP potential arising from the bare grating itself:

$$V_{\text{grating}}(x) = -\frac{\hbar}{16\pi^2\epsilon_0 x^3} \int_0^\infty d\xi \, \alpha^A(i\xi) \frac{\epsilon(i\xi) - 1}{\epsilon(i\xi) + 1}, \quad (29)$$

where $\alpha^A(i\xi)$ is given by (20) and

$$\epsilon(\omega) = \frac{\Omega_L^2 - \omega^2 - i\omega\gamma_L}{\Omega_T^2 - \omega^2 - i\omega\gamma_T}. \quad (30)$$

We consider a grating made of silicon nitride, where the resonance frequency of longitudinal mode $\Omega_L = 2.69 \times 10^{16}$ rad/s, the resonance frequency of the transverse mode $\Omega_T = 1.33 \times 10^{16}$ rad/s, the longitudinal mode damping $\gamma_L = 3.05 \times 10^{16}$ rad/s, and the transverse mode damping $\gamma_T = 6.40 \times 10^{15}$ rad/s [53].

To obtain the effect of the CP potentials on transmission signal and fringe visibility, we substitute

$$V(x) = V_{\text{grating}}(x + x_o) + V_{\text{grating}}(x_o - x)$$
$$+ V_{\text{coat}}(x + x_o) + V_{\text{coat}}(x_o - x) \quad (31)$$

into (14), and compute (16) and (17). The cutoff distance x_c can again be evaluated using (23) and (24).

Due to the limited availability of data regarding rotatory strength, electric, and magnetic anisotropy factors of molecules in chemistry, we base our following simulations on a reasonable estimate of molecular properties to see the trends. Since the CP force from the coating is generally weak compared to that from the grating itself, we proceed under the assumption that the grating is characterized by a thickness of grating $b = 160$ nm, a reduced periodicity $d = 80$ nm, a shorter grating distance $L = 10$ mm, an open fraction $f = 0.45$, and coating thickness of $a = 10$ nm.

Figure 3(i) depicts the simulation where $|R_{01}| = 1000 \times 10^{-40}$ cgs, $g_e = 0.2$, and $g_m = 5$ for both matter-wave molecules and molecules coating the second grating G_2. For (ii), it is assumed that $|R_{01}| = 5000 \times 10^{-40}$ cgs, $g_e = 0.3$, and $g_m = 3.3$ for both molecules. We set the transition frequency $\omega_1 = 2\pi \times 10^{15}$ s^{-1}, the number density of the coating molecules $n_B = 5 \times 10^{28}$/m^3 and $m = 1000$ Da for the molecules traveling as matter waves. The second grating is always coated with right-handed molecules. As depicted in the figure, we only observe a small difference between both enantiomers in the transmission signal. This is hard to measure in an experiment and motivates us to expand our analysis to the case where chiral coatings are additionally applied to both the first and the third grating. We demonstrate that this can improve the overall chiral selectivity of the interferometer.

V. ALL GRATINGS COATED BY CHIRAL MOLECULES

Here, we assume to have three identical SiN gratings, all coated with a layer of enantiomer pure, right-handed ($R_{01}^B > 0$) molecules, while all other parameters are the same as in the previous section. As before, the molecules see a combination of electric, magnetic, and chiral CP forces from the coating, as well as electric CP forces from the grating, resulting in the interferogram and fringe visibility as illustrated in Fig. 4.
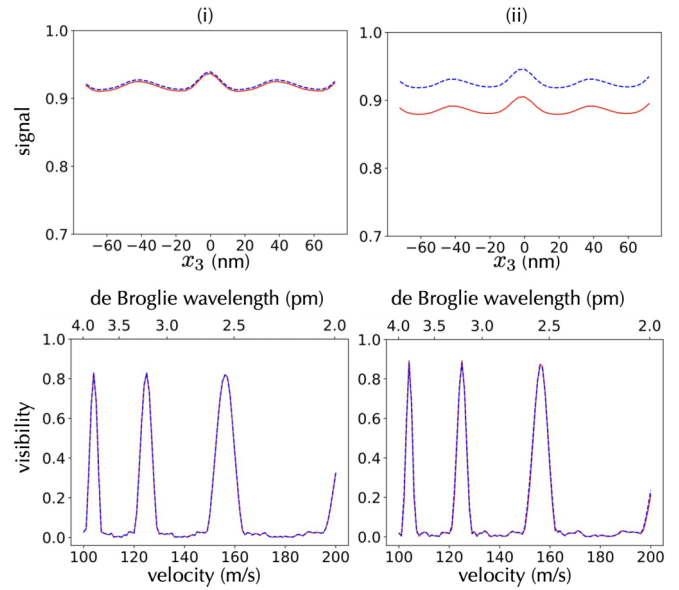

FIG. 3. Interferometer transmission (top) and fringe visibility (bottom) compared for right-handed (solid red line) and left-handed (dashed blue line) molecules. The simulation is done for (i) molecules with $|R_{01}| = 1000 \times 10^{-40}$ cgs, $g_e = 0.2$, $g_m = 5$ and (ii) molecules with $|R_{01}| = 5000 \times 10^{-40}$ cgs, $g_e = 0.3$, $g_m = 3.3$. In both cases, $m = 1000$ Da and $\omega_1 = 2\pi \times 10^{15}$ s^{-1}. In this more realistic scenario, the grating substrates are all inherently nonchiral, but G_2 is assumed to be coated by chiral molecules with a layer thickness $a = 10$ nm. The velocity $v_z = 140$ m/s in the top panels.

The panel (i) is simulated for molecules with $|R_{01}| = 1000 \times 10^{-40}$ cgs, $g_e = 0.2$, and $g_m = 5$, while panel (ii) shows the result for molecules with $|R_{01}| = 5000 \times 10^{-40}$ cgs, $g_e = 0.3$, and $g_m = 3.3$. The right-handed molecules experience a strong attractive force because the electric, magnetic, and chiral components all share the same sign. This leads to a
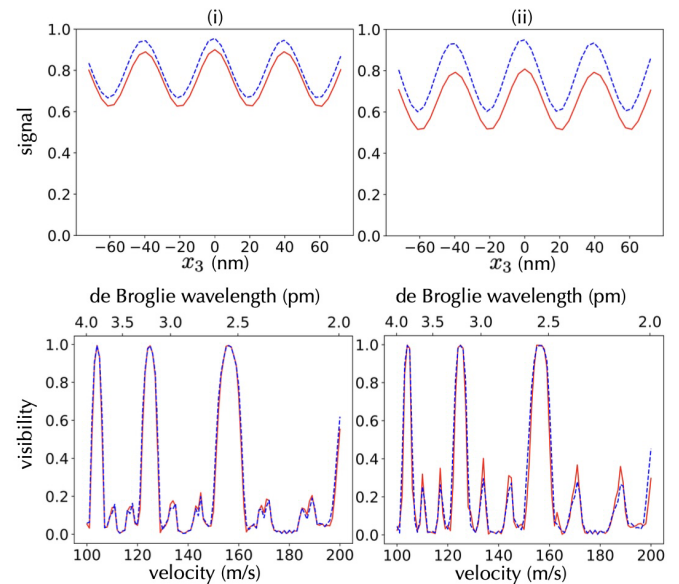

FIG. 4. Same displays as in Fig. 3, but here all gratings are identical nonchiral SiN$_x$ masks, coated with a layer of chiral molecules.
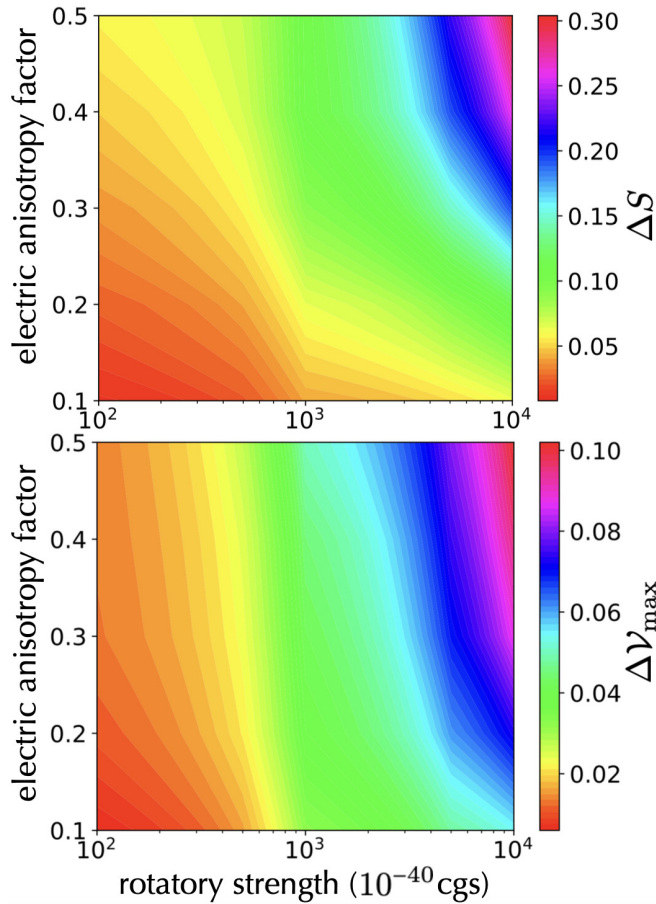
FIG. 5. The maximum difference in the mean transmission signal (upper panel) and the maximum difference in fringe visibility (lower panel) between the two enantiomers are plotted as a function of the molecular rotatory strength and its electric anisotropy factor g_e. The maximum is found across all velocities from 100 to 200 m/s, averaging over a resolution of 10 m/s.

reduction in the effective grating slit width and to a loss of molecules near the coatings. Figure 4 thus demonstrates that a coating of chiral molecules to all gratings can yield an observable effect of chiral CP forces in the transmission signal. Values close to our simulation parameters can be obtained for tailored molecules, such as [4]CC [54,55].

To explore a comprehensive range of potential test molecules, we plot in the upper panel of Fig. 5 the difference in mean interferometer *transmission signals,*

$$\Delta S = \frac{1}{4fd} \int_{-2fd}^{2fd} [S^L(x_3) - S^R(x_3)]/S^L(x_3)\, dx_3, \qquad (32)$$

as a function of the rotatory strength R_{01} and the electric anisotropy factor g_e. Here, S_L and S_R are the transmission signals of the left-handed and right-handed molecules, respectively. The lower panel of Fig. 5 shows the corresponding maximum difference in fringe *visibility* $\Delta \mathcal{V}_{max}$. Our simulations capture the maximum values across a molecular velocity range from $v_z = 100$ to 200 m/s, and they allow for an experimental velocity resolution of $\Delta v_z = 10$ m/s. This provides clear guidance for possible experiments, as soon as molecular parameters of a given species are exactly known.

Note that the magnetic component of the CP force is generally negligible compared to the electric and the chiral components of the CP force. Here we assume that $m = 1000$ Da and $\omega_1 = 2\pi \times 10^{15}$ s^{-1}. The effects of the chiral CP force are more best seen in the transmission signal but also apparent in the fringe visibility. A particularly distinct difference between enantiomers becomes apparent for molecules with a rotatory strength $>10^{-37}$ cgs and $g_e > 0.1$. In the existing literature, it has been reported that molecules such as [4]CC can demonstrate a rotatory strength exceeding 10^{-37} cgs [54–56], and molecules such as 3-methyl-cyclopentanone exhibit g_e values exceeding 0.1 [57]. We anticipate that data pertaining to these parameters for various molecules will become more accessible in the future.

VI. EXPERIMENTAL ASPECTS

Talbot-Lau interferometers with nanomechanical gratings have been realized previously with electrons [58], positrons [59], atoms [60], and molecules [30,33]. The interferometer technology is demanding but well under control. We therefore focus on the specific requirements for the observation of chiral dispersion forces. This requires the realization of chiral gratings and beams of molecules with large optical rotatory strength such as [4]CC.

Gratings could be coated by self-assembled monolayers of chiral substances. This may be suitable for narrow gratings and one can even orient all molecules within such a layer [61–63]. For larger and mechanically robust structures, dip coating is a feasible technology. For structures in the 100 nm range, however, surface tension is a challenge in all wet-chemical processes with nanostructures, and needs to be addressed [64]. We also need many mono-layers for the proposed work. Vapor deposition [65,66] is conceivable for hexahelicene and 3-methylcyclopentanone but still needs to be experimentally verified for [4]CC. We also assume the absence of local surface charges, which may dephase matter waves of polar molecules in transit through a nanograting [32]. While several highly chiral molecules, such as [4]CC, are not expected to have a permanent electric dipole moment in their thermal ground state, molecular modeling suggests that conformers with dipole moments up to 5 debye may transiently develop on the timescale of nanoseconds. This can be suppressed by launching the molecules into a cryogenic buffer gas to freeze out all vibrational dynamics [67].

VII. CONCLUSION

We have examined three scenarios in which chiral CP forces can influence the transmission signal and the visibility of chiral molecules behind a Talbot-Lau matter-wave interferometer with nanogratings. When the second grating consists of a perfectly chiral nanostructure ($r_c \to 1$, $r \to 0$), a small chiral effect should be observed even for the realistic case of hexahelicene, and a very pronounced effect would be expected if we found a molecule with ten times larger rotatory strength (Fig. 2). Since such nanochiral materials are experimentally demanding, we have considered the case where the second grating G_2 is coated with highly chiral substances. We have identified examples of molecular

rotatory strengths and asymmetry factors that would make an observable difference in molecular transmission but only a small difference in matter-wave fringe visibility (Fig. 3). The effect can be enhanced by applying the chiral coating to all gratings (Fig. 4) since even gratings that do not contribute to the interferometer phase shift influence the transmission and contrast by an effective slit narrowing. In this case, effects become visible already when both the coating molecules and matter-wave molecules possess a rotatory strength $>10^{-37}$ cgs and an electric anisotropy factor $g_e > 0.1$ (Fig. 4). Again the transmission is more affected than the fringe visibility. Finally, we have analyzed interference figures for the same experimental geometry but for molecules now varying vastly in their rotatory strength (10^{-38}–10^{-36} cgs) and in their electric anisotropy factor (0.1–0.5), and samples from an experimentally plausible velocity range (100–200 m/s) with finite band width (10 m/s). Figure 5 thus reveals the influence of these

molecular parameters, and, while differences in transmission and fringe visibility of 1% may still be resolved, effects on the level of 10% would be clearly accessible. The molecular parameters are certainly challenging, but not unfeasible, and the proposed experiment may allow probing for the first time the effect of *static chiral* Casimir-Polder forces on isolated and here even delocalized molecules.

[1] H. B. G. Casimir and D. Polder, The influence of retardation on the London–van der Waals Forces, Phys. Rev. **73**, 360 (1948).

[2] R. Zhao, J. Zhou, Th. Koschny, E. N. Economou, and C. M. Soukoulis, Repulsive Casimir force in chiral metamaterials, Phys. Rev. Lett. **103**, 103602 (2009).

[3] Q. Jiang and F. Wilczek, Chiral Casimir forces: Repulsive, enhanced, tunable, Phys. Rev. B **99**, 125403 (2019).

[4] D. T. Butcher, S. Y. Buhmann, and S. Scheel, Casimir–Polder forces between chiral objects, New J. Phys. **14**, 113013 (2012).

[5] P. Barcellona, H. Safari, A. Salam, and S. Y. Buhmann, Enhanced chiral discriminatory van der Waals Interactions mediated by chiral surfaces, Phys. Rev. Lett. **118**, 193401 (2017).

[6] F. Suzuki, T. Momose, and S. Y. Buhmann, Stern-Gerlach separator of chiral enantiomers based on the Casimir-Polder potential, Phys. Rev. A **99**, 012513 (2019).

[7] H. Safari, P. Barcellona, S. Y. Buhmann, and A. Salam, Medium-assisted van der Waals dispersion interactions involving chiral molecules, New J. Phys. **22**, 053049 (2020).

[8] J. Trost and K. Hornberger, Hund's Paradox and the collisional stabilization of chiral molecules, Phys. Rev. Lett. **103**, 023202 (2009).

[9] B. A. Stickler, M. Diekmann, R. Berger, and D. Wang, Enantiomer superpositions from matter-wave interference of chiral molecules, Phys. Rev. X **11**, 031056 (2021).

[10] W. H. Zurek, *Decoherence and Quantum Darwinism: From Quantum Foundations to Objective Classical Reality* (Cambridge University Press, Cambridge, in press).

[11] A. Guijarro and M. Yus, *The Origin of Chirality in the Molecules of Life* (Royal Society of Chemistry, Cambridge, 2009).

[12] R. Naaman, Y. Paltiel, and D. H. Waldeck, Chiral induced spin selectivity gives a new twist on spin-control in chemistry, Acc. Chem. Res. **53**, 2659 (2020).

[13] A. Ghazaryan, M. Lemeshko, and A. G. Volosniev, Filtering spins by scattering from a lattice of point magnets, Commun. Phys. **3**, 178 (2020).

[14] X. Li *et al.*, Proximity-induced chiral quantum light generation in strain-engineered WSe$_2$/NiPS$_3$ heterostructures, Nat. Mater. **22**, 1311 (2023).

[15] A. Forde, D. Ghosh, D. Kilin, A. C. Evans, S. Tretiak, and A. J. Neukirch, Induced chirality in halide perovskite

clusters through surface chemistry, J. Phys. Chem. Lett. **13**, 686 (2022).

[16] A. Yokoyama, M. Yoshida, A. Ishii, and Y. K. Kato, Giant circular dichroism in individual carbon nanotubes induced by extrinsic chirality, Phys. Rev. X **4**, 011005 (2014).

[17] C. Ye, Q. Zhang, Y.-Y. Chen, and Y. Li, Determination of enantiomeric excess with chirality-dependent ac Stark effects in cyclic three-level models, Phys. Rev. A **100**, 033411 (2019).

[18] J. C. Franz, S. Y. Buhmann, and A. Salam, Macroscopic quantum electrodynamics theory of resonance energy transfer involving chiral molecules, Phys. Rev. A **107**, 032809 (2023).

[19] R. P. Cameron, S. M. Barnett, and A. M. Yao, Discriminatory optical force for chiral molecules, New J. Phys. **16**, 013020 (2014).

[20] N. Kravets, A. Aleksanyan, and E. Brasselet, Chiral optical Stern-Gerlach Newtonian experiment, Phys. Rev. Lett. **122**, 024301 (2019).

[21] I. Tutunnikov, E. Gershnabel, S. Gold, and I. S. Averbukh, Selective orientation of chiral molecules by laser fields with twisted polarization, J. Phys. Chem. Lett. **9**, 1105 (2018).

[22] A. A. Milner, J. A. M. Fordyce, I. MacPhail-Bartley, W. Wasserman, V. Milner, I. Tutunnikov, and I. Sh. Averbukh, Controlled enantioselective orientation of chiral molecules with an optical centrifuge, Phys. Rev. Lett. **122**, 223201 (2019).

[23] C. Genet, Chiral light–chiral matter interactions: An optical force perspective, ACS Photonics **9**, 319 (2022).

[24] R. E. Grisenti, W. Schöllkopf, J. P. Toennies, G. C. Hegerfeldt, and T. Köhler, Determination of atom-surface van der Waals potentials from transmission-grating diffraction intensities, Phys. Rev. Lett. **83**, 1755 (1999).

[25] R. Brühl, P. Fouquet, R. E. Grisenti, J. P. Toennies, G. C. Hegerfeldt, T. Köhler, M. Stoll, and C. Walter, The van der Waals potential between metastable atoms and solid surfaces: Novel diffraction experiments vs. theory, Europhys. Lett. **59**, 357 (2002).

[26] V. P. A. Lonij, C. E. Klauss, W. F. Holmgren, and A. D. Cronin, Atom diffraction reveals the impact of atomic core electrons on atom-surface potentials, Phys. Rev. Lett. **105**, 233202 (2010).

[27] C. Garcion, N. Fabre, H. Bricha, F. Perales, S. Scheel, M. Ducloy, and G. Dutier, Intermediate-range Casimir-Polder

interaction probed by high-order slow atom diffraction, Phys. Rev. Lett. **127**, 170402 (2021).

[28] Q. Bouton, G. Dutier, N. Fabre, E. Charron, C. Garcion, N. Gaaloul, and L. Julien, Quantum description of atomic diffraction by material nanostructures, arXiv:2312.12818.

[29] M. Arndt, O. Nairz, J. Voss-Andreae, C. Keller, G. van der Zouw, and A. Zeilinger, Wave–particle duality of C_{60} molecules, Nature (London) **401**, 680 (1999).

[30] B. Brezger, L. Hackermüller, S. Uttenthaler, J. Petschinka, M. Arndt, and A. Zeilinger, Matter-wave interferometer for large molecules, Phys. Rev. Lett. **88**, 100404 (2002).

[31] C. Brand, M. Sclafani, C. Knobloch, Y. Lilach, T. Juffmann, J. Kotakoski, C. Mangler, A. Winter, A. Turchanin, J. Meyer, O. Cheshnovsky and M. Arndt, An atomically thin matter-wave beamsplitter, Nat. Nanotechnol. **10**, 845 (2015).

[32] C. Knobloch, B. A. Stickler, C. Brand, M. Sclafani, Y. Lilach, T. Juffmann, O. Cheshnovsky, K. Hornberger, M. Arndt, On the role of the electric dipole moment in the diffraction of biomolecules at nanomechanical gratings, Fortschr. Phys. **65**, 1600025 (2017).

[33] T. Juffmann, S. Truppe, P. Geyer, A. G. Major, S. Deachapunya, H. Ulbricht, and M. Arndt, Wave and particle in molecular interference lithography, Phys. Rev. Lett. **103**, 263601 (2009).

[34] K. Hornberger, J. E. Sipe, and M. Arndt, Theory of decoherence in a matter wave Talbot-Lau interferometer, Phys. Rev. A **70**, 053608 (2004).

[35] Y. Y. Fein, F. Kiałka, P. Geyer, S. Gerlich, and M. Arndt, Coriolis compensation via gravity in a matter-wave interferometer, New J. Phys. **22**, 033013 (2020).

[36] S. Nimmrichter, P. Haslinger, K. Hornberger, and M. Arndt, Concept of an ionizing time-domain matter-wave interferometer, New J. Phys. **13**, 075002 (2011).

[37] T. Juffmann, A. Milic, M. Müllneritsch, P. Asenbaum, A. Tsukernik, J. Tüxen, M. Mayor, O. Cheshnovsky, and M. Arndt, Real-time single-molecule imaging of quantum interference, Nat. Nanotechnol. **7**, 297 (2012).

[38] L. Hackermüller, S. Uttenthaler, K. Hornberger, E. Reiger, B. Brezger, A. Zeilinger, and M. Arndt, Wave nature of biomolecules and fluorofullerenes, Phys. Rev. Lett. **91**, 090408 (2003).

[39] M. Strauß, A. Shayeghi, M. F. X. Mauser, P. Geyer, T. Kostersitz, J. Salapa, O. Dobrovolskiy, S. Daly, J. Commandeur, Y. Hua, V. Köhler, M. Mayor, J. Benserhir, C. Bruschini, E. Charbon, M. Castaneda, M. Gevers, R. Gourgues, N. Kalhor, A. Fognini, and M. Arndt, Highly sensitive single-molecule detection of macromolecule ion beams, Sci. Adv. **9**, eadj2801 (2023).

[40] J. Lekner, Optical properties of isotropic chiral media, Pure Appl. Opt. **5**, 417 (1996).

[41] S. Scheel and S. Buhmann, Macroscopic quantum electrodynamics - concepts and applications, Acta Phys. Slovaca **58**, 675 (2008).

[42] S. Y. Buhmann, *Dispersion Forces I: Macroscopic Quantum Electrodynamics and Ground-State Casimir, Casimir-Polder and van der Waals Forces* (Springer, Berlin, 2012).

[43] S. M. Ali, T. M. Habashy, and J. A. Kong, Spectral-domain dyadic Green's function in layered chiral media, J. Opt. Soc. Am. A **9**, 413 (1992).

[44] C. Brand, J. Fiedler, T. Juffmann, M. Sclafani, C. Knobloch, S. Scheel, Y. Lilach, O. Cheshnovsky, and M. Arndt, A Green's

function approach to modeling molecular diffraction in the limit of ultra-thin gratings, Ann. Phys. (Berlin) **527**, 580 (2015).

[45] K. Simonovic, R. Ferstl, A. Barlow, A. Shayeghi, C. Brand, and M. Arndt, Impact of molecular properties on diffraction at nanomasks with low charge density, arXiv:2401.05854.

[46] S. Nimmrichter and K. Hornberger, Theory of near-field matter-wave interference beyond the eikonal approximation, Phys. Rev. A **78**, 023612 (2008).

[47] J. Fiedler and B. Holst, An atom passing through a hole in a dielectric membrane: Impact of dispersion forces on mask-based matter-wave lithography, J. Phys. B **55**, 025401 (2022).

[48] I. Warnke and F. Furche, Circular dichroism: Electronic, WIREs Comput. Mol. Sci. **2**, 150 (2012).

[49] J. A. Schellman, Circular dichroism and optical rotation, Chem. Rev. **75**, 323 (1975).

[50] A. P. McCauley *et al.*, Microstructure effects for Casimir forces in chiral metamaterials, Phys. Rev. B **82**, 165108 (2010).

[51] D. L. Andrews, D. P. Craig, and T. Thirunamachandran, Molecular quantum electrodynamics in chemical physics, Int. Rev. Phys. Chem. **8**, 339 (1989).

[52] A. Salam, *Molecular Quantum Electrodynamics: Long-Range Intermolecular Interactions* (Wiley, Hoboken, NJ, 2010).

[53] S. Y. Buhmann, S. Scheel, S. Å. Ellingsen, K. Hornberger, and A. Jacob, Casimir-Polder interaction of fullerene molecules with surfaces, Phys. Rev. A **85**, 042513 (2012).

[54] S. Sato, A. Yoshii, S. Takahashi, S. Furumi, M. Takeuchi, and H. Isobe, Chiral intertwined spirals and magnetic transition dipole moments dictated by cylinder helicity, Proc. Natl. Acad. Sci. USA **114**, 13097 (2017).

[55] K. Kogashi, T. Matsuno, S. Sato, and H. Isobe, Narrowing segments of helical carbon nanotubes with curved aromatic panels, Angew. Chem. Int. Ed. **58**, 7385 (2019).

[56] Y. Onaka, S. Tanaka, A. Kobayashi, T. Matsuno, and H. Isobe, A large-bore chiral cylindrical molecule prone to radial deformations, Tetrahedron Lett. **96**, 153774 (2022).

[57] D. Kröner, Chiral distinction by ultrashort laser pulses: Electron wavepacket dynamics incorporating magnetic interactions, J. Phys. Chem. A **115**, 14510 (2011).

[58] B. J. McMorran and A. D. Cronin, An electron Talbot interferometer, New J. Phys. **11**, 033021 (2009).

[59] S. Sala, A. Ariga, A. Ereditato, R. Ferragut, M. Giammarchi, M. Leone, C. Pistillo, and P. Scampoli, First demonstration of antimatter wave interferometry, Sci. Adv. **5**, eaav7610 (2019).

[60] J. F. Clauser and S. Li, Talbot-vonLau atom interferometry with cold slow potassium, Phys. Rev. A **49**, R2213(R) (1994).

[61] J. C. Love, L. A. Estroff, J. K. Kriebel, R. G. Nuzzo, and G. M. Whitesides, Self-assembled monolayers of thiolates on metals as a form of nanotechnology, Chem. Rev. **105**, 1103 (2005).

[62] P. V. Möllers, S. Ulku, D. Jayarathna, F. Tassinari, D. Nürenberg, R. Naaman, C. Achim, and H. Zacharias, Spin-selective electron transmission through self-assembled monolayers of double-stranded peptide nucleic acid, Chirality **33**, 93 (2021).

[63] B. Göhler, V. Hamelbeck, T. Z. Markus, M. Kettner, G. F. Hanne, Z. Vager, R. Naaman, and H. Zacharias, Spin selectivity in electron transmission through self-assembled monolayers of double-stranded DNA, Science **331**, 894 (2011).

[64] M. Robertson-Tessi, R. J. Wild, A. D. Cronin, and Tim Savas, Cleaning silicon nitride gratings with liquid immersion, J. Vac. Sci. Technol. B **24**, 1409 (2006).

[65] P. M. Martin, *Handbook of Deposition Technologies for Films and Coatings* (Elsevier, Norwich, NY, 2009).

[66] H. Al-Bustami, S. Khaldi, O. Shoseyov, S. Yochelis, K. Killi, I. Berg, E. Gross, Y. Paltiel, and R. Yerushalmi, Atomic and molecular layer deposition of chiral thin films show-

ing up to 99% spin selective transport, Nano Lett. **22**, 5022 (2022).

[67] J. Piskorski, D. Patterson, S. Eibenberger, and J. M. Doyle, Cooling, spectroscopy and non-sticking of trans-Stilbene and Nile Red, ChemPhysChem **15**, 3800 (2014).